Simultaneous Intensity Bias Estimation and Stripe Noise Removal in Infrared Images Using the Global and Local Sparsity Constraints

Li Liu, Luping Xu, and Houzhang Fang

***Abstract*— Infrared (IR) images are often contaminated by obvious intensity bias and stripes, which severely affect the visual quality and subsequent applications. It is challenging to eliminate simultaneously the mixed nonuniformity noise without blurring the fine-image details in low-textured IR images. In this article, we present a new model for simultaneous intensity bias correction and destriping through introducing two sparsity constraints. One is that model fit on the intensity bias should be as accurate as possible. A bivariate polynomial model is built to characterize the global smoothness of the intensity bias. The other constraint is that the unidirectional variational sparse model can concisely represent the direction characteristic of stripe noise. A computationally efficient numerical algorithm based on split Bregman iteration is used to solve the complex optimization problem. The proposed method is fundamentally different from the existing denoising techniques and simultaneously estimates the sharp image, intensity bias, and stripe components. Significant improvement on image quality is achieved on both simulated and real studies. Both qualitative and quantitative comparisons with the state-of-the-art correction methods demonstrate its superiority.**

***Index Terms*— Destriping, infrared (IR) imaging, intensity bias correction, optimization-based model, sparsity.**

I. Introduction

INFRARED (IR) imaging systems are widely used in military and civilian applications, including remote sensing, astronomy imaging, automatic target recognition, and video surveillance. However, the performance of IR imaging systems is severely affected by nonuniformity noise. One kind of common nonuniformity noise, such as stripe noise, is mainly due to the nonuniform response of the individual detectors, dark currents, and differences within the readout electronics. The other kind is generated by the temperature fluctuations of the optical lens and other mechanical components of IR imaging systems. This type of nonuniformity noise is spatially continuous, and its magnitude significantly varies with temperature fluctuation. The superimposed effects of stripe and intensity bias are shown in Fig. 1(a). Since it is difficult to fix the complicated nonuniformity noise on the hardware design, our research aim is to study the effective and efficient image processing methods to compensate for the hardware defects of the IR detectors.

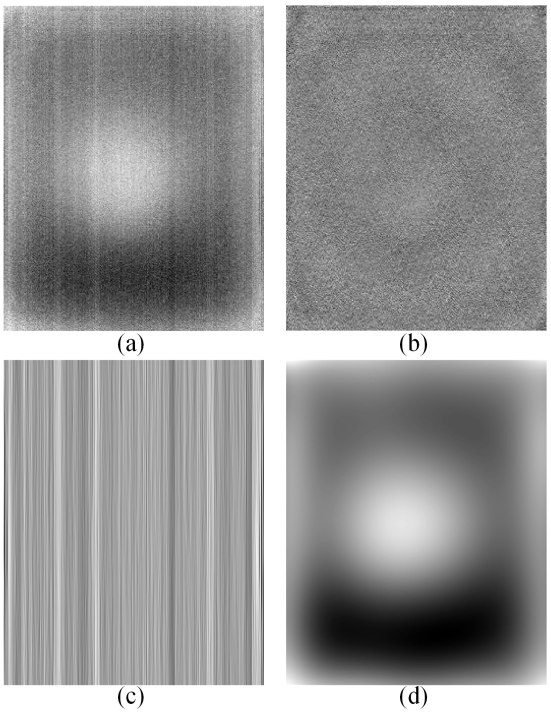


Fig. 1. Accurate extraction of stripe and bias components from a real noisy IR image. (a) Raw IR image. (b) Random noise in Fig. 1(a). (c) Stripe noise in Fig. 1(a). (d) Intensity bias in Fig. 1(a).

In video-based surveillance systems, nonlinear behaviors of IR detectors generate significant stripe noise in the captured IR images, which results in high-frequency image artifacts. Meanwhile, temperature fluctuations of lens and other mechanical components will cause a smooth intensity bias in its output images, and the phenomenon becomes particularly obvious when the IR camera is imaging a low-contrast scene [1]. In airborne remote sensing, when an aircraft flies at high speed, the optics temperature-dependent nonuniformity effects of IR imaging systems also cause high-magnitude intensity bias.

Manuscript received March 8, 2019; revised October 14, 2019; accepted October 17, 2019. Date of publication November 18, 2019; date of current version February 26, 2020. This work was supported in part by the Fundamental Research Funds for the Central Universities under Grant JBX171305, in part by the Aeronautical Science Foundation under Grant ASFC-20170181002, and in part by the National Natural Science Foundation of China under Grant 61801355, Grant 41501371, and Grant 61433007. *(Corresponding author: Li Liu.)*

L. Liu and L. Xu are with the School of Aerospace Science and Technology, Xidian University, Xi'an 710071, China (e-mail: dr.liliu@hotmail.com; mail2111@163.com).

H. Fang is with the School of Computer Science and Technology, Xidian University, Xi'an 710071, China (e-mail: houzhangfang@xidian.edu.cn).

Color versions of one or more of the figures in this article are available online at http://ieeexplore.ieee.org.

Digital Object Identifier 10.1109/TGRS.2019.2948601

0196-2892 © 2019 IEEE. Personal use is permitted, but republication/redistribution requires IEEE permission.
See https://www.ieee.org/publications/rights/index.html for more information.

Authorized licensed use limited to: XIDIAN UNIVERSITY. Downloaded on February 28,2020 at 03:05:26 UTC from IEEE Xplore. Restrictions apply.

This type of nonuniformity noise induced by background IR window emission can significantly degrade the signal-to-noise ratio and even drive the detector into saturation [2]. In addition, in spaceborne remote sensing, both stripe noise and intensity bias yielded by inhomogeneous pixel responsivities significantly degrade the quality of the captured IR images and affect subsequent high-level image processing tasks, such as image deconvolution, image registration, and object identification. This poses a severe problem in the detection of remote targets in IR search and track (IRST). Therefore, it is essential to conduct the nonuniformity correction (NUC) method to remove the false alarms in IRST.

A. IR Image-Destriping Methods

To date, a large number of destriping algorithms have been proposed. In general, they can be categorized into several main categories. The first category is reference-based approaches, such as the two-point calibration [3]. This kind of approach is simple but more restrictive and requires a standard uniform radiation source. In the real-time applications, the nonuniformity tends to drift slowly with time due to the instability of the IR focal-plane arrays. In addition, the optics temperature-dependent nonuniformity effects of the IR imaging systems degrade the image quality further. Thus, these factors severely impair the effectiveness of one-time laboratory-derived NUC. Unlike general visualization applications, advanced airborne or spaceborne IR imaging systems achieve a high-precision and high-efficiency NUC at the expense of a repeated in-flight calibration, which means the imaging operation must be halted. Therefore, this method is not suitable for real-time IR applications.

Filtering-based approaches, such as Fourier [4] or wavelet-Fourier domain filter [5], constitute another type of destriping algorithms. These methods can effectively remove the periodic stripes in IR images by truncating the specific stripe component in a transformed domain, because the periodic property of the stripes can be easily identified and extracted in the transformed domain. Limited by the truncating operation, this algorithm will falsely indicate that image details with amplitudes less than the threshold are treated as stripe noise and removed. The stripe noise with an amplitude greater than the threshold is regarded as image edge and retained. To conquer this drawback, a 1-D guided filter is applied to extract the stripe noise components from the high-frequency signals (containing both strip noise and image texture) [6]. Only the estimated noise components are subtracted from the raw IR images to remove the stripe noise without significant blurring or ringing artifacts.

Recently, researchers have paid much attention on the optimization-based models. Regarding the destriping issue as an ill-posed inverse problem, these approaches make use of prior information to extract the stripe component from the degraded image and have made significant progress. A maximum-*a posteriori* correction model with a Huber–Markov prior was proposed in [7] to solve the destriping and inpainting problems. A more sophisticated model was designed by making use of the unidirectional structure information of stripe noise [8], and has been successfully used to estimate detector biases in MODIS thermal emissive bands [9]. To remove stripe and random noise simultaneously, a unified variational framework with unidirectional total variation (UTV) and sparse representation over learned dictionary was presented [10]. More recently, a low-rank-based single-image decomposition model was proposed to separate the original image information from the stripe component perfectly by incorporating the characteristics of both the stripe noise and the remote sensing images [11]. Though the above-mentioned methods have achieved encouraging destriping performance, they still face great challenges when dealing with mixed nonuniformity noise.

B. IR Bias-Correction Methods

To estimate intensity bias in IR images, there also exist various methods. The first significant class is based on spatial filtering and spectral filtering, with trying to remove the sharp changes of the image and, thus, resulting in a smoothly changing intensity bias [12], [13]. The filtering-based methods have an intrinsic disadvantage. That is, it is difficult to select a threshold both in the spatial and spectral domains appropriately to differentiate the intensity changes between the latent IR image and the intensity bias. Although the multiscale filtering method in [14] can improve the performance of the correction algorithm, its performance is still restricted, especially in the IR images with complex background noise.

The second major class of methods is based on intensity- or gradient-domain fitting. A bihexic function was used to model the spurious contrast in the intensity domain, which was introduced by nonuniform heating from the flash lamp, vignetting due to the camera, lateral heat diffusion, and other effects [15]. Another method learns to differentiate the derivatives of the ideal IR image and intensity bias. A single-image-based method was proposed to compute optics temperature-dependent intensity bias by using a gradient-domain fitting model [1]. In addition, the estimated intensity bias was directly subtracted from the raw IR image to remove the optics-related intensity variations. However, as the image size increases and background noise becomes complex, the modified bilateral filter used in [1] can significantly affect its efficiency and effectiveness. A similar correction model was built to estimate the gradients caused by the interior radiation noise according to the fixed spatial low-frequency information in multiframe images [16].

The third creative class tries to tackle the intensity bias noise in a variational framework. This method considers enough of the salient characteristics of real degraded IR images. An alternating minimization method is applied to solve the nonconvex energy function in order to estimate the intensity bias and the latent image [2]. Both correction residue and computational efficiency show its superior performance. Recently, a new NUC method based on a deep multiscale residual network was presented—the first one to tackle the mixed nonuniformity noise of stripe and intensity bias [17]. Although this method has a better performance in the simulated-data experiment, it lacks enough results from real-data experiments.

Authorized licensed use limited to: XIDIAN UNIVERSITY. Downloaded on February 28,2020 at 03:05:26 UTC from IEEE Xplore. Restrictions apply.

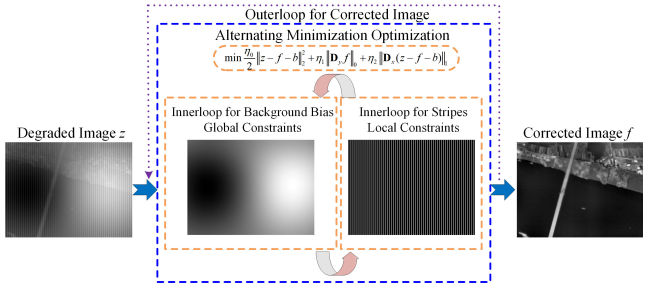


Fig. 2. Framework of the proposed method.

C. Proposed Method

Although numerous NUC methods have been proposed in the past decades, most of them are designed for only one specific task, such as image destriping or intensity bias correction, and cannot effectively solve the complex mixed nonuniformity noise in Fig. 1(a). This article presents a different processing angle to simultaneously estimate and separate the stripe noise component and the intensity bias component from low-textured IR noisy images. Inspired by the successes of optimization-based methods, we propose an NUC method for both stripe and intensity bias separation and removal by fully considering the salient characteristics of the stripes and the intensity biases. Two constraints are incorporated in the proposed method. From the local perspective, the smoothness along the stripes and the discontinuity across the stripes are both analyzed and modeled on the ℓ_1-norm and ℓ_0-norm regularization terms, respectively. In addition, from the global one, the fit model of intensity bias, viz., the large-scale nonuniformity noise, is expected to be as concise as possible. In our scheme, a bivariate polynomial model is used to characterize the global smoothness of intensity bias. In order to tackle the complex nonconvex ℓ_0-norm minimization, a computationally efficient numerical algorithm based on split Bregman iteration is introduced. The framework of the proposed method is shown in Fig. 2. The resulting optimization problem is split into two subproblems that can be easily solved. The main ideas and contributions of the proposed approach are summarized as follows.

1) Different from the single optimization model of intensity bias estimation or destriping in IR data, we construct an unified correction model to tackle the mixed nonuniformity issue simultaneously. In order to estimate the large-scale intensity bias and the small-scale stripe noise, the global and local sparsity constraints are considered. The proposed model can effectively reduce correction residual and preserve fine-image details well.
2) The split Bregman iterative algorithm (SBIA) is applied to decompose the complex ℓ_2-ℓ_0-ℓ_1 norm minimization problem into two simpler subproblems. Due to its fast convergence and superior numerical stability, our method has achieved faster testing speed.
3) The proposed method has been tested on both simulated and real IR data. Compared with previous methods, our method has obtained better correction performance.

The remainder of this article is organized as follows. In Section II, we discuss the correction model based on the global and local sparsity constraints. In Section III, we introduce a fast iterative method to solve the proposed model. In Section IV, we present and analyze the experimental results. Finally, we summarize this article in Section V.

II. Variational Model

A. Problem Formulation

In this article, we consider an IR image to be a 2-D bounded variation function. The intensity bias and the stripe noise are assumed to be additive [2], [10], [18], [31]. Mathematically, the degradation model can be stated as follows:

$$z = f + b + s \tag{1}$$

where z and f are the degraded image and the sharp image, respectively, b denotes the intensity bias, and s is the stripe noise and random noise. Our primary aim is to estimate the sharp image f from the degradation model (1). It is obviously an ill-posed problem, because the number of unknowns is triple the number of equations. Therefore, additional information is required.

B. Correction Model

To tackle the ill-posed problem effectively, the key task is to explore the properties of intensity bias and stripe and to describe them in appropriate constraint terms to constitute an optimization model. More specifically, the global smoothness property is fully considered to estimate the large-scale intensity bias, and the local variational property is deliberated to extract the small-scale stripe component.

1) Global Smoothness of Intensity Bias: In general, the large-scale intensity biases in the IR images are spatially smooth. To estimate b, there are basically two methods: nonparametric method and parametric method. The nonparametric method does not assume any model on b and enforces spatially local smoothness on adjacent pixels. Therefore, the regularization term on b can be expressed as $\|\mathbf{L}b\|$, where $\mathbf{L}$ denotes the second- or high-order derivative operator. Though the local smoothness of intensity bias b can be successfully applied in image vignetting [19] and uneven intensity correction of remote sensing images [20], strong random noise from IR detectors can significantly degrade the effectiveness of the above-mentioned local regularization term. However, the parametric method represents b with some model functions and estimates the parameters of the model. We try to make the model as concise as possible. Thus, to improve the robustness of the proposed method, a bivariate polynomial model in K degree is chosen for its efficiency and expressed as follows:

$$b(x_i, y_i) = \sum_{t=0}^{K} \sum_{s=0}^{K-t} a_{t,s} x_i^t y_i^s = \mathbf{Wa} \tag{2}$$

where (x_i, y_i) denotes the coordinates of pixel i, $\mathbf{a}$ is the column vector form of $a_{t,s}$, and $\mathbf{W}$ denotes the row vectors holding the monomial terms. Since the parametric model can accurately describe both the local and global smoothness, it can effectively improve the estimation precision of b.

Authorized licensed use limited to: XIDIAN UNIVERSITY. Downloaded on February 28,2020 at 03:05:26 UTC from IEEE Xplore. Restrictions apply.

As $\mathbf{D}$ is a gradient operator, the x-component, $\mathbf{D}_x b$ can be expressed as a linear combination of model parameters $\mathbf{a}$

$$\mathbf{D}_x b = \sum_{t=0}^{K} \sum_{s=0}^{K-t} a_{t,s} \left(x_i^t - x_{i'}^t\right) y_i^s = c_{x,i}^T \mathbf{a} \tag{3}$$

where i' is the left neighbor pixel of i. Thus, $\mathbf{D}_x b$ can be expressed as

$$\mathbf{D}_x b = \mathbf{C}_x \mathbf{a} \tag{4}$$

where $\mathbf{C}_x$ is a constant matrix formulated by treating $c_{x,i}^T$ in (3) as one of its rows.

2) Local Continuity of Latent IR Image: Numerous statistical analyses of IR images [2], [21], [22] have shown that the image gradients of IR scenes can be better modeled with sparse distribution, e.g., hyper-Laplacian. When adding column-by-column stripes to the latent image, the image gradients across the stripes at the stripe locations are much greater than the ones at the nonstripe locations. Thus, the local continuity of f is broken. In the severely degraded images, the discontinuity across the stripes is a very salient local property. Recently, ℓ_0 gradient minimization has been widely applied in image denoising [23] and image restoration [24]. The ℓ_0 sparse analysis priors are consistently found to perform more effectively, and as a high-sparsity-pursuiting regularizer preserve salient intensity changes better. Therefore, we design the following regularization term:

$$R_1 = \|\mathbf{D}_y f\|_0 \tag{5}$$

where $\mathbf{D}_y$ denotes the gradient operator in the across-stripe direction.

3) Local Smoothness Along Stripe Direction: The stripes in the IR images generally appear along the horizontal or vertical direction. The intensities of the adjacent pixels in a single stripe have relatively small variations, that is, the stripes have a salient property of local smoothness. Since the gradients describe the variations of adjacent pixels, the local smoothness can be constrained by minimizing the gradients along the stripe [11], [25]. Therefore, we construct another term as

$$R_2 = \|\mathbf{D}_x(z - f - b)\|_1 \tag{6}$$

where $\mathbf{D}_x$ denotes the gradient operator in the along-stripe direction.

In the above-mentioned analysis, we fully investigate the intensity bias and stripe noise from the global and local perspectives and, finally, obtain three salient characteristics, viz., the global smoothness of intensity bias, the local continuity of the latent IR image, and the local smoothness in the along-stripe direction. Combining these properties, an unified model to simultaneously tackle intensity bias and stripe noise is constructed as follows:

$$\mathbf{min}\ \frac{\eta_0}{2}\|z-f-b\|_2^2+\eta_1\|\mathbf{D}_y f\|_0+\eta_2\|\mathbf{D}_x(z-f-b)\|_1 \tag{7}$$

where η_0, η_1, and η_2 are the positive parameters and b is equal to $\mathbf{Wa}$. Since the model in (7) already incorporates the spatial smoothness on b, the smoothness constraints on b can be eliminated.

III. Split Bregman Optimization

Due to the nondifferentiability and nonseparability of the proposed model (7), it is necessary to apply an efficient algorithm to solve this nonconvex and nonsmooth optimization model. Recently, the SBIA has been successfully used in solving several regularized optimization problems [26]–[29]. Since the SBIA has the fast convergence and the superior numerical stability, it is competitive when compared with many of the state-of-the-art methods for constrained optimization. Therefore, we apply the SBIA to solve the proposed model (7).

The proposed model aims to optimize two variables simultaneously, which can be solved by an alternatively minimizing strategy. Thus, our model can be split into two minimization subproblems

$$\mathbf{min}_b\ \frac{\eta_0}{2}\|z-f-b\|_2^2+\eta_2\|\mathbf{D}_x(z-f-b)\|_1 \tag{8}$$

and

$$\mathbf{min}_f\ \frac{\eta_0}{2}\|z-f-b\|_2^2+\eta_1\|\mathbf{D}_y f\|_0+\eta_2\|\mathbf{D}_x(z-f-b)\|_1. \tag{9}$$

A. Estimating b With f

The basic idea of the SBIA is to convert the unconstrained minimization subproblem on b into a constrained one by introducing an auxiliary variable $\mathbf{d}_1 = \mathbf{D}_x(z - f - b)$, as follows:

$$\begin{aligned} &\mathbf{min}\ \frac{\eta_0}{2}\|z-f-b\|_2^2+\eta_2\|\mathbf{d}_1\|_1 \\ &\mathbf{s.t.}\quad \mathbf{d}_1 = \mathbf{D}_x(z-f-b) \end{aligned} \tag{10}$$

by strictly enforcing the constraint and applying the Bregman iteration; the problem (10) can further be transformed into a nonconstrained minimization

$$\begin{aligned} \mathbf{min}\ &\frac{\eta_0}{2}\|z-f-b\|_2^2+\eta_2\|\mathbf{d}_1\|_1 \\ &+\frac{\alpha}{2}\|\mathbf{d}_1-\mathbf{D}_x(z-f-b)-\mathbf{s}_1\|_2^2 \end{aligned} \tag{11}$$

where α denotes the penalization parameter and $\mathbf{s}_1$ is a Bregman variable.

The b-related subproblem is given by

$$\mathbf{min}\ \eta_0\|z-f-b\|_2^2+\alpha\|\mathbf{d}_1-\mathbf{D}_x(z-f-b)-\mathbf{s}_1\|_2^2 \tag{12}$$

which is a least-square problem. According to the above analysis in Section II, b and $\mathbf{D_x}b$ can be expressed as $\mathbf{Wa}$ and $\mathbf{C}_x\mathbf{a}$, respectively. Thus, it is equivalent to the following linear system:

$$\mathbf{min}\ \eta_0\|z-f-\mathbf{Wa}\|_2^2+\alpha\|\mathbf{d}_1-\mathbf{D}_x(z-f)+\mathbf{C}_x\mathbf{a}-\mathbf{s}_1\|_2^2 \tag{13}$$

and the closed-form solution for this least squares minimization problem is

$$\begin{aligned} \mathbf{a} = &\left(\eta_0\mathbf{W}^T\mathbf{W}+\alpha\mathbf{C}_x^T\mathbf{C}_x\right)^{-1} \\ &\times[\eta_0\mathbf{W}^T(z-f)+\alpha\mathbf{C}_x^T(\mathbf{D}_x(z-f)-\mathbf{d}_1+\mathbf{s}_1)]. \end{aligned} \tag{14}$$

In addition, the $\mathbf{d}_1$-related subproblem is

$$\mathbf{min}\ \eta_2\|\mathbf{d}_1\|_1+\frac{\alpha}{2}\|\mathbf{d}_1-\mathbf{D}_x(z-f-b)-\mathbf{s}_1\|_2^2 \tag{15}$$

Authorized licensed use limited to: XIDIAN UNIVERSITY. Downloaded on February 28,2020 at 03:05:26 UTC from IEEE Xplore. Restrictions apply.

which can be solved by using a shrinkage operator as follows:

$$\mathbf{d}_1 = \text{shrink}\left(\mathbf{D}_x(z - f - b) + \mathbf{s}_1, \frac{\eta_2}{\alpha}\right) \tag{16}$$

where

$$\text{shrink}(\mu, \lambda) = \frac{\mu}{|\mu|} * \max(|\mu| - \lambda, 0). \tag{17}$$

Finally, we update the Bregman variable $\mathbf{s}_1$

$$\mathbf{s}_1' = \mathbf{s}_1 + \mathbf{D}_x(z - f - \mathbf{Wa}) - \mathbf{d}_1. \tag{18}$$

B. Estimating f With b

Minimizing with respect to f can be done in a similar fashion. By introducing two auxiliary variables $\mathbf{d}_2 = \mathbf{D}_y f$ and $\mathbf{d}_3 = \mathbf{D}_x(z_1 - f)$, we convert (9) into

$$\begin{aligned} &\textbf{min } \frac{\eta_0}{2}\|z_1 - f\|_2^2 + \eta_1\|\mathbf{d}_2\|_0 + \eta_2\|\mathbf{d}_3\|_1 \\ &\textbf{s.t. } \mathbf{d}_2 = \mathbf{D}_y f, \mathbf{d}_3 = \mathbf{D}_x(z_1 - f) \end{aligned} \tag{19}$$

where z_1 is equal to $z - b$. Applying SBIA again results in the following minimization subproblem:

$$\begin{aligned} \textbf{min } \frac{\eta_0}{2}\|z_1 - f\|_2^2 + \eta_1\|\mathbf{d}_2\|_0 + \frac{\beta}{2}\|\mathbf{d}_2 - \mathbf{D}_y f - \mathbf{s}_2\|_2^2 \\ + \eta_2\|\mathbf{d}_3\|_1 + \frac{\gamma}{2}\|\mathbf{d}_3 - \mathbf{D}_x(z_1 - f) - \mathbf{s}_3\|_2^2 \end{aligned} \tag{20}$$

where β and γ denote the penalization parameters, and $\mathbf{s}_2$ and $\mathbf{s}_3$ are the Bregman variables.

The f-related subproblem is given by

$$\begin{aligned} \textbf{min } \eta_0\|z_1 - f\|_2^2 + \beta\|\mathbf{d}_2 - \mathbf{D}_y f - \mathbf{s}_2\|_2^2 \\ + \gamma\|\mathbf{d}_3 - \mathbf{D}_x(z_1 - f) - \mathbf{s}_3\|_2^2. \end{aligned} \tag{21}$$

In addition, for periodic images, the closed-form solution for this least squares minimization problem is

$$f = \mathcal{F}^{-1}\left(\frac{A}{\eta_0 + \beta\mathcal{F}(\mathbf{D}_y^T\mathbf{D}_y) + \gamma\mathcal{F}(\mathbf{D}_x^T\mathbf{D}_x)}\right) \tag{22}$$

where

$$A = \eta_0\mathcal{F}(z_1) + \beta\mathcal{F}\left(\mathbf{D}_y^T(\mathbf{d}_2 - \mathbf{s}_2)\right) + \gamma\mathcal{F}\left(\mathbf{D}_x^T(\mathbf{D}_x z_1 + \mathbf{s}_3 - \mathbf{d}_3)\right). \tag{23}$$

$\mathcal{F}$ denotes the 2-D Fourier transform, and $\mathcal{F}^{-1}$ denotes the 2-D inverse Fourier transform.

The $\mathbf{d}_2$-subproblem is given by

$$\textbf{min } \eta_1\|\mathbf{d}_2\|_0 + \frac{\beta}{2}\|\mathbf{d}_2 - \mathbf{D}_y f - \mathbf{s}_2\|_2^2. \tag{24}$$

Note that (24) is a pixelwise minimization problem; thus, $\mathbf{d}_2$ is obtained based on [30]

$$\mathbf{d}_2 = \begin{cases} \mathbf{D}_y f + \mathbf{s}_2, & |\mathbf{D}_y f + \mathbf{s}_2|^2 > \dfrac{2\eta_1}{\beta} \\ 0, & \text{otherwise.} \end{cases} \tag{25}$$

Moreover, the $\mathbf{d}_3$-related subproblem is given by

$$\begin{aligned} \textbf{min} &= \eta_2\|\mathbf{d}_3\|_1 + \frac{\gamma}{2}\|\mathbf{d}_3 - \mathbf{D}_x(z_1 - f) - \mathbf{s}_3\|_2^2 \\ \mathbf{d}_3 &= \text{shrink}\left(\mathbf{D}_x(z_1 - f) + \mathbf{s}_3, \frac{\eta_2}{\gamma}\right). \end{aligned} \tag{26}$$

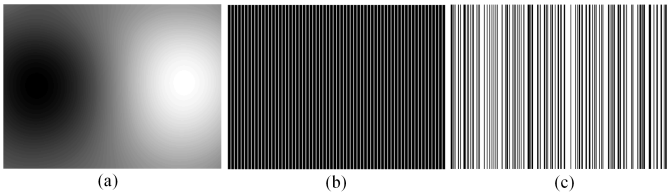


Fig. 3. Simulated mixed nonuniformity noise. (a) Intensity bias. (b) Periodic stripe noise. (c) Nonperiodic stripe noise.

Finally, we update the Bregman variable $\mathbf{s}_2$ and $\mathbf{s}_3$

$$\begin{aligned} \mathbf{s}_2' &= \mathbf{s}_2 + \mathbf{D}_y f - \mathbf{d}_2 \\ \mathbf{s}_3' &= \mathbf{s}_3 + \mathbf{D}_x(z_1 - f) - \mathbf{d}_3. \end{aligned} \tag{27}$$

IV. Experimental Results and Discussion

In this section, we focus on impartially evaluating the performance of the proposed correction method, since few researchers have paid their attention to the mixed nonuniformity issue in the IR images. To demonstrate the effectiveness of the proposed model, we compared it with a variety of state-of-the-art NUC methods, including UTV-based NUC [8], anisotropic spectral–spatial total variation (ASSTV) model [31], low-rank image decomposition (LRID) [11], and gradient-filtering (GF) NUC [1]. The first three models are used to remove the stripe noise and the last one is applied to estimate the intensity bias.

A. Simulated Experiment

In the simulated experiment, we added both the variable intensity bias and distinct stripe on the IR images of different scenes. First, after the background noise of the captured IR images is analyzed fully, the degradation model of the intensity bias can be expressed as follows:

$$b(x_i, y_i) = k_0 \cdot y_i \cdot e^{-x_i^2 - y_i^2} \tag{28}$$

where k_0 is a scalar weight and (x_i, y_i) is the coordinate of the ith pixel. Second, two types of stripe noises, viz., periodic and nonperiodic stripes, are superimposed on the IR images with intensity bias. The simulated intensity bias, periodic stripe, and nonperiodic stripe are shown in Fig. 3, respectively.

1) Periodic Stripe and Intensity Bias: We generated the IR image with intensity bias by the degradation model (28) and then added periodic stripes on it. Fig. 4(a) shows a raw IR image of the suburban area, and the degraded image is shown in Fig. 4(b). Since the single state-of-the-art NUC method cannot effectively solve the mixed noise issue, the combinations of the destriping methods and the intensity bias-correction method are applied in this experiment in order to impartially evaluate their performance.

The experimental results are shown in Fig. 4(c)–(f). It is observed from the image regions marked by the red ellipse in Fig. 4(c)–(f) that the proposed method outperforms the state-of-the-art ones with respect to removing stripes and intensity bias, preserving image details and minimizing artifacts. The greatest disadvantage of the combinational correction model is the interinfluence of intensity bias and stripe

Authorized licensed use limited to: XIDIAN UNIVERSITY. Downloaded on February 28,2020 at 03:05:26 UTC from IEEE Xplore. Restrictions apply.

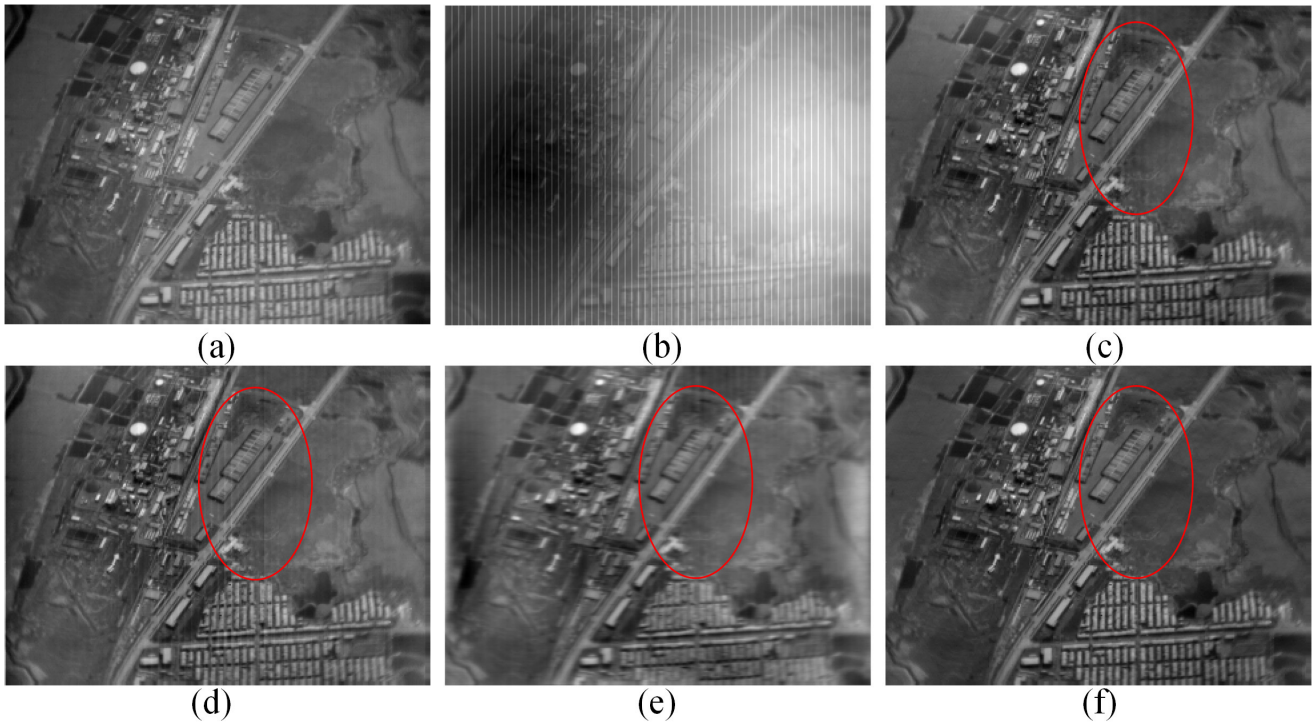


Fig. 4. Efficient and accurate solution for simultaneous bias estimation and periodic stripe removal. (a) Original image. (b) Degraded image. (c) UTV+GF. (d) ASSTV+GF. (e) LRID+GF. (f) Proposed.

on estimation accuracy. Specifically speaking, gradient priors are widely used in the process of estimating the stripe or the bias, as they have been shown to be effective in suppressing artifacts. However, the gradients of the stripes have a severe influence on the GF model, because the gradient filter, viz., the modified bilateral filter in [1], cannot effectively remove all the gradients of the stripes, and conversely the complex intensity bias also significantly deteriorates the performance of the destriping methods. Accordingly, the performance of the combinational NUC methods is inevitably subject to limitation. Although the intensity biases are estimated well, the residual stripes in the central part of Fig. 4(c) and (d) are observed evidently. LRID performs poorly, since the strong mixed nonuniformity noise, shown in Fig. 3, does not meet the low-rank property of the stripes. Both residual noise and blur effects are significant in Fig. 4(e). The proposed method obtains a better visual performance for the mixed nonuniformity noise in Fig. 4(f). Fig. 5(a) and (b) shows an original IR image of the bridge and its degraded image, respectively. It is clearly observed in Fig. 5(c)–(f) that the LRID has the largest nonuniformity residue, since it is not suitable for the removal of the mixed nonuniformity noise. Compared with the other three combinational correction methods, the proposed method obtains the smallest nonuniformity residue and well preserves image texture characteristics.

2) Nonperiodic Stripe and Intensity Bias: Since the nonperiodic stripes widely exist in the captured IR images, we perform another simulated experiment to test the effectiveness of the different NUC methods in removing both nonperiodical stripes and intensity biases. In this experiment, the locations and intensities of each stripe line are randomly distributed on the whole image. The comparative results of different NUC methods are shown in Figs. 6 and 7. The combination of UTV and GF can obtain better performance than ASSTV and GF. It is obvious that the residual stripes, marked by the red ellipse in Figs. 6(c) and 7(c), are smaller than those in Figs. 6(d) and 7(d). In Figs. 6(e) and 7(e), the residual stripes exist obviously. The image details are blurred by the combination of LRID and GF, and image structures in the border are heavily destroyed. However, in Figs. 6(f) and 7(f), both stripes and intensity bias are perfectly removed by the proposed method without introducing any noticeable artifacts.

From the above-mentioned analysis, we can find that the proposed method is robust to both strong intensity bias and stripe, and performs much better than other correction methods in terms of image structure preserving, bias estimation, and stripe removal. This is mainly because the following holds. First, a significant advantage of the proposed model for estimating background bias is to adaptively determine the smoothness degree for the estimated bias. The intensity bias may be underestimated or overestimated if the smoothness degree cannot be guessed correctly by the user. Second, all priors are based on the salient structure characteristics of the intensity bias and the stripe.

3) Quantitative Evaluation: It is not enough to evaluate the performance only by visual observation. Hence, to demonstrate the robustness of our method in the presence of periodic and nonperiodic stripes, and intensity bias, the quantitative assessments including the peak signal-to-noise ratio (PSNR) and the structural similarity index (SSIM) [32] values are reported in Tables I and II, respectively. The larger the PSNRs and SSIMs are, the higher the image quality is. The highest

Authorized licensed use limited to: XIDIAN UNIVERSITY. Downloaded on February 28,2020 at 03:05:26 UTC from IEEE Xplore. Restrictions apply.

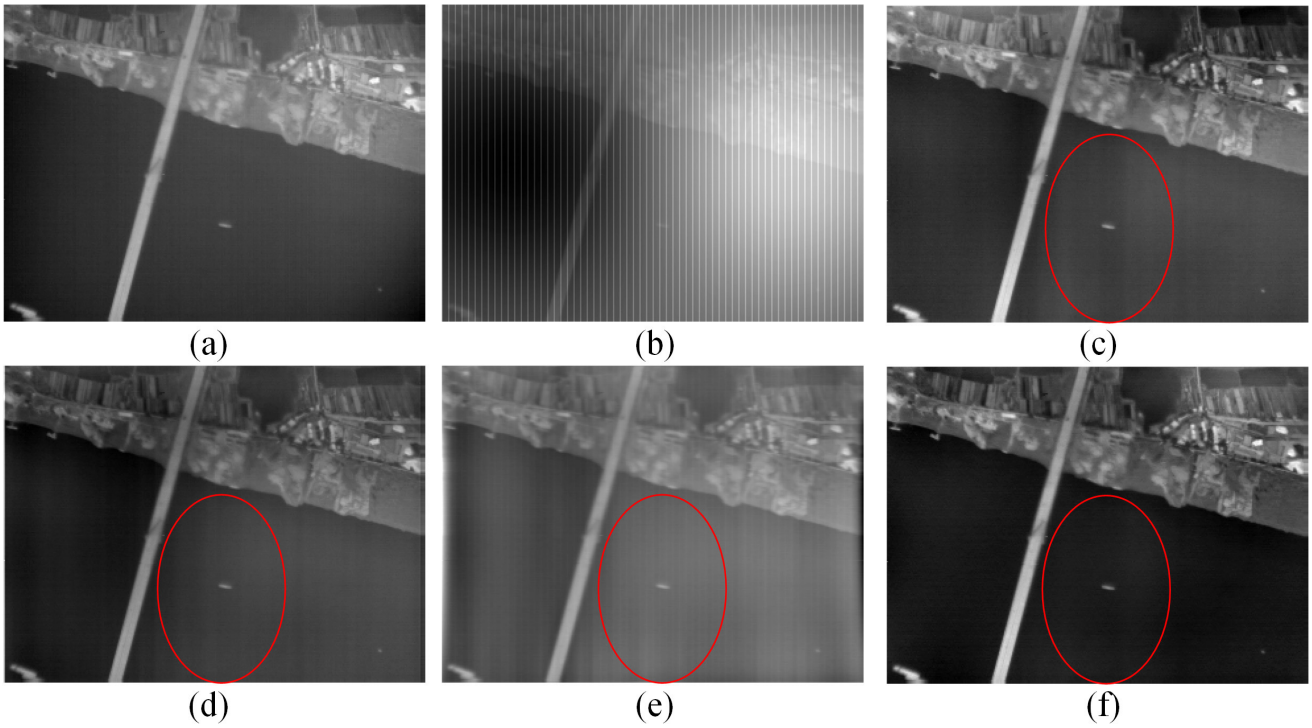


Fig. 5. Efficient and accurate solution for simultaneous bias estimation and periodic stripe removal. (a) Original image. (b) Degraded image. (c) UTV+GF. (d) ASSTV+GF. (e) LRID+GF. (f) Proposed.

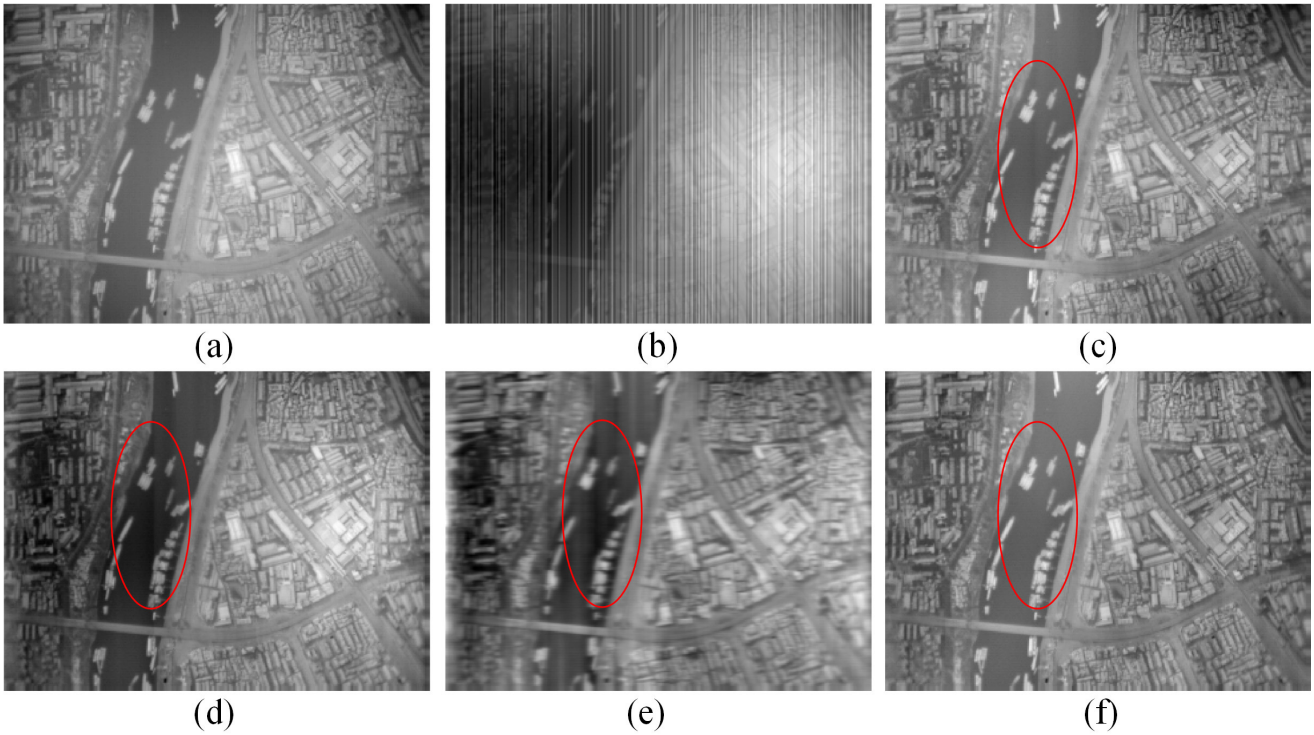


Fig. 6. Efficient and accurate solution for simultaneous bias estimation and nonperiodic stripe removal. (a) Original image. (b) Degraded image. (c) UTV+GF. (d) ASSTV+GF. (e) LRID+GF. (f) Proposed.

PSNR and SSIM values for each image and each noise level are highlighted in bold. In all the experiments, the bit number of the pixel is 16. The constant values from original images and simulated intensity bias are removed due to their adverse impact on the final results. We have the following observations. First, the proposed method achieves the highest PSNR

Authorized licensed use limited to: XIDIAN UNIVERSITY. Downloaded on February 28,2020 at 03:05:26 UTC from IEEE Xplore. Restrictions apply.

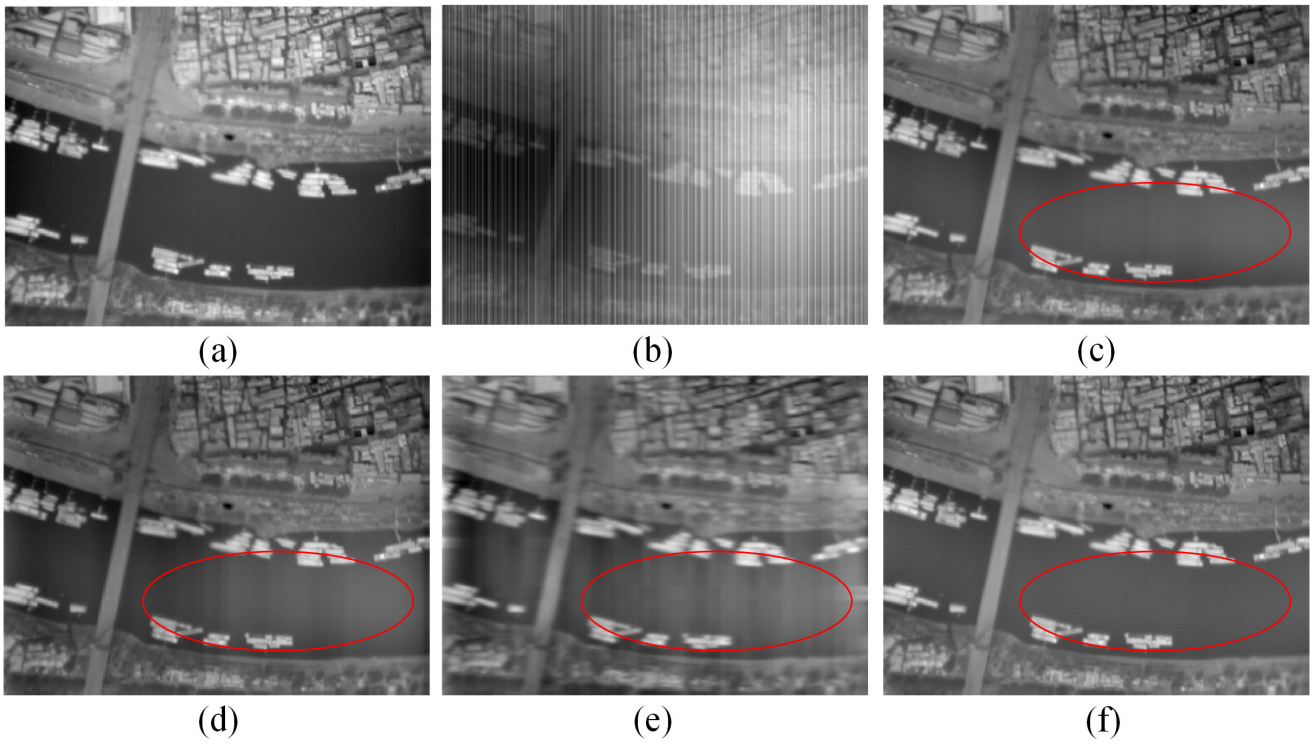


Fig. 7. Efficient and accurate solution for simultaneous bias estimation and nonperiodic stripe removal. (a) Original image. (b) Degraded image. (c) UTV+GF. (d) ASSTV+GF. (e) LRID+GF. (f) Proposed.

TABLE I
PSNRs OF THE ORIGINAL IMAGES AND THE IMAGES CORRECTED BY DIFFERENT NUC ALGORITHMS

Image	Method	Periodic Stripe and Variant Intensity Bias						Non-periodic Stripe and Variant Intensity Bias					
Suburb	Degraded	26.98	26.64	25.63	25.35	24.46	24.22	24.82	24.22	22.61	22.14	21.00	20.77
	UTV+GF	51.26	51.26	51.23	51.04	50.18	50.18	50.92	50.92	50.83	50.83	50.71	50.71
	ASSTV+GF	51.72	51.40	49.72	51.31	51.51	51.13	51.69	51.41	51.66	51.44	51.53	51.17
	LRID+GF	50.04	50.02	49.92	49.86	49.77	49.73	49.88	49.78	49.42	49.15	49.29	49.21
	Proposed	**52.82**	**53.44**	**53.38**	**53.08**	**53.45**	**52.88**	**53.12**	**53.11**	**52.74**	**52.39**	**52.37**	**52.32**
Bridge	Degraded	25.67	25.38	24.49	24.25	23.45	23.25	24.82	24.22	22.62	22.18	21.16	20.77
	UTV+GF	50.92	50.92	50.62	50.62	50.30	50.32	51.23	51.16	50.33	50.30	51.04	51.05
	ASSTV+GF	50.93	50.71	50.80	50.48	50.59	50.42	51.56	51.37	50.85	50.91	51.44	51.24
	LRID+GF	49.78	49.78	49.34	49.39	48.94	48.92	49.70	49.59	49.76	49.70	49.27	49.19
	Proposed	**52.51**	**52.46**	**52.44**	**52.48**	**52.45**	**52.43**	**53.57**	**53.66**	**52.92**	**52.35**	**53.29**	**53.22**
River Harbor	Degraded	25.86	25.57	24.67	24.42	23.61	23.39	25.22	24.62	23.12	22.64	21.42	20.91
	UTV+GF	46.74	45.55	46.54	46.54	46.32	46.32	46.35	46.35	45.70	46.27	46.15	46.15
	ASSTV+GF	45.69	45.55	45.44	45.26	45.18	45.57	46.12	46.07	45.75	45.79	45.51	45.43
	LRID+GF	45.02	45.01	44.75	44.75	44.50	44.49	45.23	45.19	44.83	44.78	44.40	44.36
	Proposed	**47.66**	**47.37**	**47.76**	**47.38**	**47.76**	**47.46**	**47.54**	**47.48**	**47.52**	**47.49**	**47.57**	**47.41**
Urban Area	Degraded	27.18	27.00	26.46	26.31	25.74	25.48	24.60	23.79	23.61	22.84	21.98	20.69
	UTV+GF	44.70	44.70	44.57	44.57	44.91	44.98	44.91	44.91	44.81	44.81	44.70	44.70
	ASSTV+GF	45.45	45.44	44.75	45.26	45.73	45.11	45.64	45.59	45.55	45.50	45.38	45.31
	LRID+GF	43.01	43.01	42.38	42.85	43.31	43.59	43.29	43.38	43.15	43.24	43.08	42.91
	Proposed	**45.58**	**45.58**	**45.51**	**45.62**	**45.76**	**45.51**	**45.75**	**45.67**	**45.67**	**45.63**	**45.61**	**45.36**

and SSIM values in every noise case. Second, the proposed method has the equally excellent performance in two sets of noise cases. Third, with the increase in nonuniformity noise, the advantage of the proposed method surpasses other state-of-the-art NUC methods. This proves that the proposed method is more robust to the mixed NU noise than other methods.

Authorized licensed use limited to: XIDIAN UNIVERSITY. Downloaded on February 28,2020 at 03:05:26 UTC from IEEE Xplore. Restrictions apply.

TABLE II
SSIMs OF THE ORIGINAL IMAGES AND THE IMAGES CORRECTED BY DIFFERENT NUC ALGORITHMS

Image	Method	Periodic Stripe and Intensity Bias						Non-periodic Stripe and Intensity Bias					
Suburb	Degraded	0.0579	0.0293	0.0535	0.0271	0.0497	0.0253	0.0405	0.0314	0.0196	0.0169	0.0174	0.0250
	UTV+GF	0.9313	0.9313	0.9207	0.9194	0.9000	0.9000	0.9285	0.9285	0.9267	0.9264	0.9241	0.9241
	ASSTV+GF	0.9020	0.7876	0.8783	0.7844	0.8915	0.7782	0.9239	0.9078	0.9194	0.9018	0.9114	0.8898
	LRID+GF	0.6725	0.6715	0.6702	0.6686	0.6671	0.6658	0.6663	0.6555	0.6539	0.6487	0.6553	0.6453
	Proposed	**0.9375**	**0.9403**	**0.9407**	**0.9389**	**0.9403**	**0.9382**	**0.9396**	**0.9387**	**0.9372**	**0.9442**	**0.9365**	**0.9345**
Bridge	Degraded	0.0212	0.0106	0.0195	0.0099	0.0181	0.0092	0.0405	0.0314	0.0074	0.0067	0.0311	0.0250
	UTV+GF	0.8152	0.8152	0.8113	0.8113	0.8061	0.8068	0.9284	0.9273	0.8073	0.8061	0.9232	0.9236
	ASSTV+GF	0.7905	0.7816	0.7830	0.7589	0.7666	0.7802	0.9215	0.9196	0.7875	0.7762	0.9089	0.9014
	LRID+GF	0.5547	0.5205	0.5351	0.5214	0.5558	0.5215	0.6774	0.6619	0.4936	0.4690	0.6658	0.6510
	Proposed	**0.8193**	**0.8183**	**0.8176**	**0.8182**	**0.8179**	**0.8170**	**0.9475**	**0.9482**	**0.8305**	**0.8279**	**0.9455**	**0.9454**
River Harbor	Degraded	0.1160	0.0676	0.1089	0.0635	0.1026	0.0600	0.1302	0.0806	0.1150	0.0719	0.1029	0.0558
	UTV+GF	0.8634	0.8337	0.8590	0.8590	0.8541	0.8541	0.8489	0.8489	0.8266	0.8468	0.8441	0.8442
	ASSTV+GF	0.8377	0.8264	0.8349	0.8202	0.8313	0.8316	0.8413	0.8362	0.8212	0.8300	0.8266	0.8197
	LRID+GF	0.7246	0.7208	0.7214	0.7182	0.7188	0.7150	0.6596	0.6565	0.6574	0.6536	0.6536	0.6495
	Proposed	**0.8893**	**0.8859**	**0.8898**	**0.8862**	**0.8890**	**0.8892**	**0.8901**	**0.8898**	**0.8906**	**0.8903**	**0.8911**	**0.8883**
Urban Area	Degraded	0.0405	0.0272	0.0333	0.0225	0.1938	0.1085	0.1804	0.1339	0.1729	0.1285	0.1235	0.0954
	UTV+GF	0.9375	0.9375	0.9360	0.9360	0.9401	0.9428	0.9401	0.9401	0.9388	0.9388	0.9375	0.9375
	ASSTV+GF	0.9338	0.9335	0.9308	0.9308	0.9382	0.9368	0.9390	0.9393	0.9376	0.9382	0.9368	0.9232
	LRID+GF	0.6749	0.6748	0.8070	0.6730	0.6785	0.8015	0.6777	0.6794	0.6761	0.6778	0.6761	0.6677
	Proposed	**0.9423**	**0.9418**	**0.9421**	**0.9415**	**0.9427**	**0.9436**	**0.9419**	**0.9421**	**0.9421**	**0.9413**	**0.9419**	**0.9397**

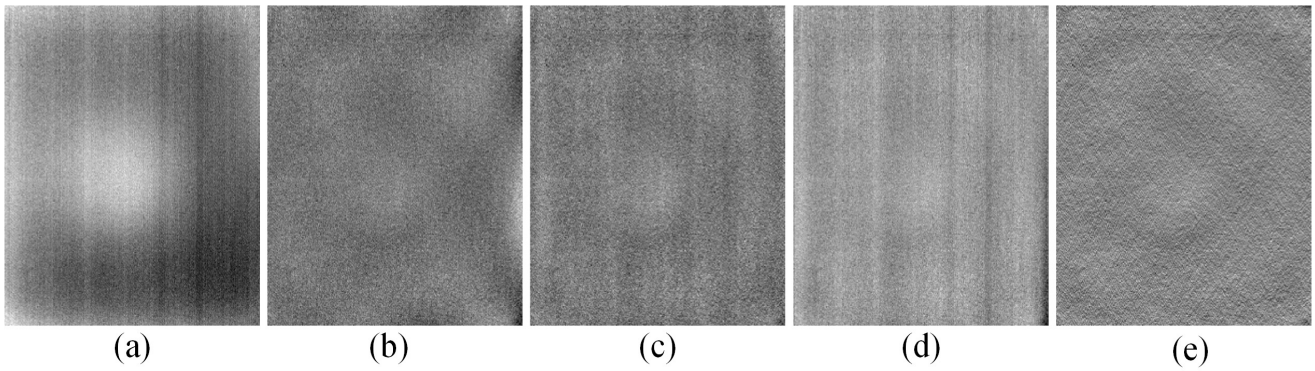


Fig. 8. Efficient and accurate solution in the real-data experiment. (a) Degraded image. (b) UTV+GF. (c) ASSTV+GF. (d) LRID+GF. (e) Proposed.

B. Real Experiment

In this section, various real-world IR data sets are used in our experiments to demonstrate the robustness and efficiency of our algorithm.

1) Nonremote Sensing Images: In this experiment, an IR camera records a uniform-temperature object, and image background is severely interfered by the superimposed effects of nonperiodic stripe and intensity bias in the record time. Fig. 8(a) shows one image frame of the captured IR video. Fig. 8(b)–(f) shows the comparative results of different correction methods. A visual assessment of these results clearly shows that the proposed approach can effectively remove both stripe and intensity bias in real IR images. The correction residues in Fig. 8(c) and (d) are more significant. Although the destripping result of UTV in Fig. 8(b) seems plausible, the bright artifacts caused by GF are obviously seen in the border of the final corrected image. The estimated stripe and bias components, shown in Fig. 9, prove the effectiveness of the proposed method further. To evaluate the corrected results in depth, a nonreference index, viz., the inverse coefficient of variation (ICV) [33], is used to give an overall quantitative assessment because of the lack of the true data in this experiment, and is defined as

$$\mathrm{ICV} = \frac{R_a}{R_{\mathrm{sd}}} \tag{29}$$

where R_a and R_{sd} are the average value and standard deviation of pixel intensities in the chosen image patch, respectively.

Authorized licensed use limited to: XIDIAN UNIVERSITY. Downloaded on February 28,2020 at 03:05:26 UTC from IEEE Xplore. Restrictions apply.

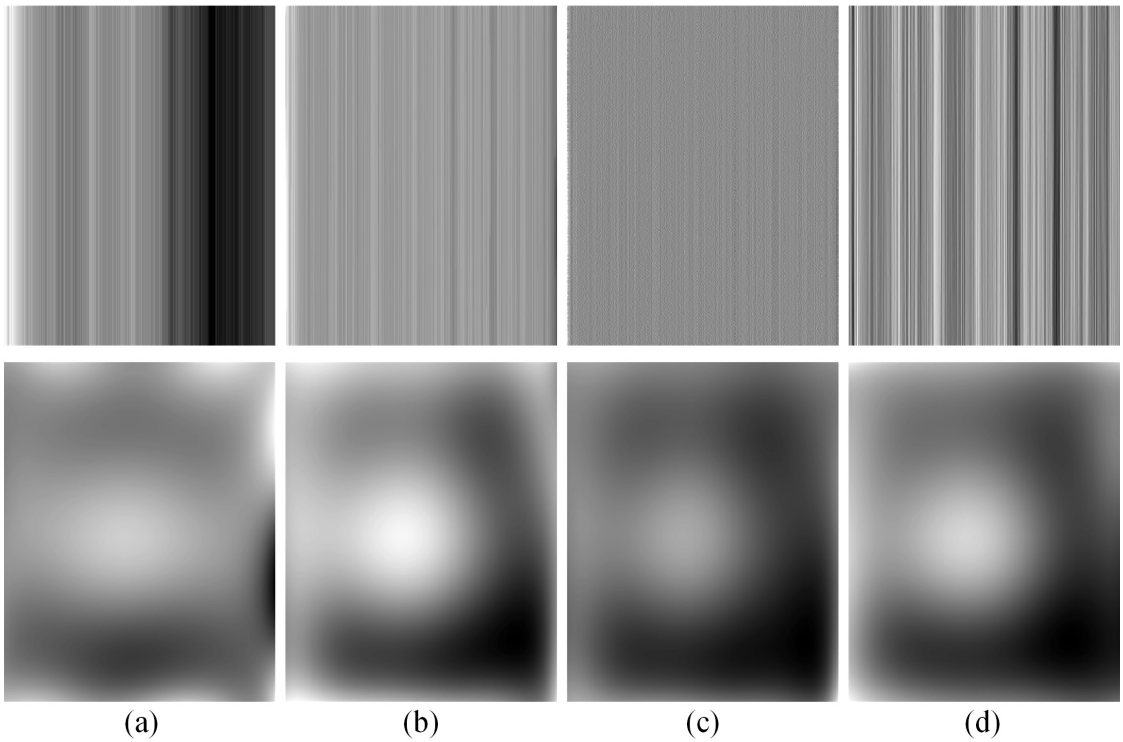


Fig. 9. Estimated stripe and bias components in Fig. (8). (a) UTV+GF. (b) ASSTV+GF. (c) LRID+GF. (d) Proposed.

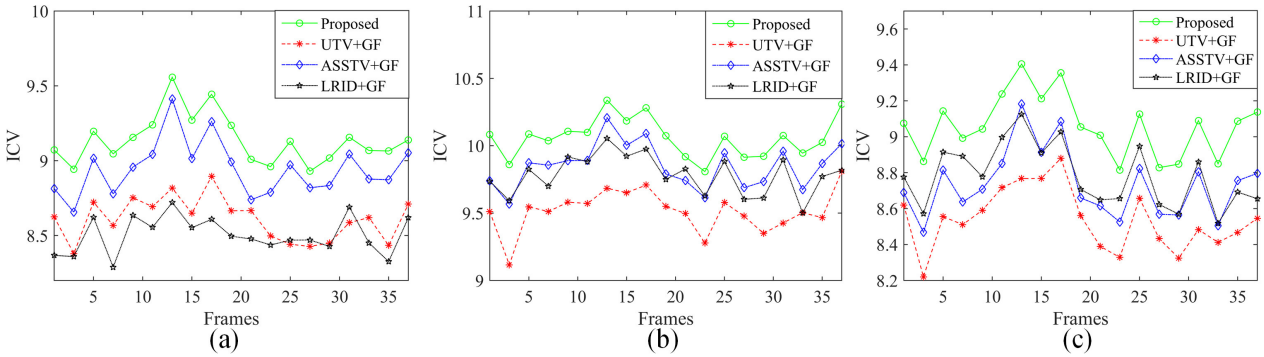


Fig. 10. ICVs of different NUC methods. (a) Image patch A. (b) Image patch B. (c) Image patch C.

The larger the ICV is, the smaller the correction residue is. For a 320 × 256 experimental image, three 50 × 256 image patches, marked A–C, are chosen to calculate the ICVs, whose center lines are located in the 50th, 150th, and 200th rows, respectively. The experimental results of the total 36 image frames are shown in Fig. 10(a)–(c). The highest ICVs of different image patches show the robustness of our method further.

2) Remote Sensing Image: A set of remote sensing IR images with a size of 1500 × 1500, shown in Fig. 11(a)–(c), are severely contaminated by nonperiodic stripe and intensity bias. The corrected images are shown in Figs. 12(a)–(d), 13(a)–(d), and 14(a)–(d), respectively. It is obviously seen that the proposed method shows much more excellent correction performance than other methods. Our method can not only tackle the stripping issue but also suppress the intensity bias of the image background. Meanwhile, the fine-image structures are well preserved. Four 100 × 1500 image patches, marked A–D, are chosen to calculate the ICVs, whose center lines are located in the 300th, 600th, 900th, and 1200th rows, respectively. The results are shown in Table III. Our method obtains the highest ICVs in the real-data experiments, which confirm the effectiveness of the proposed method. In a word, the results of the proposed method are consistent for all test images, and exhibit good visual quality with fewer artifacts than the ones obtained by the other methods.

C. Discussion

1) Parameter Determination: Equation (7) contains two terms: the reconstruction term and the regularization term. The physical meaning of the first term is to guarantee the intensity similarity between the restored image and the ground truth.

Authorized licensed use limited to: XIDIAN UNIVERSITY. Downloaded on February 28,2020 at 03:05:26 UTC from IEEE Xplore. Restrictions apply.

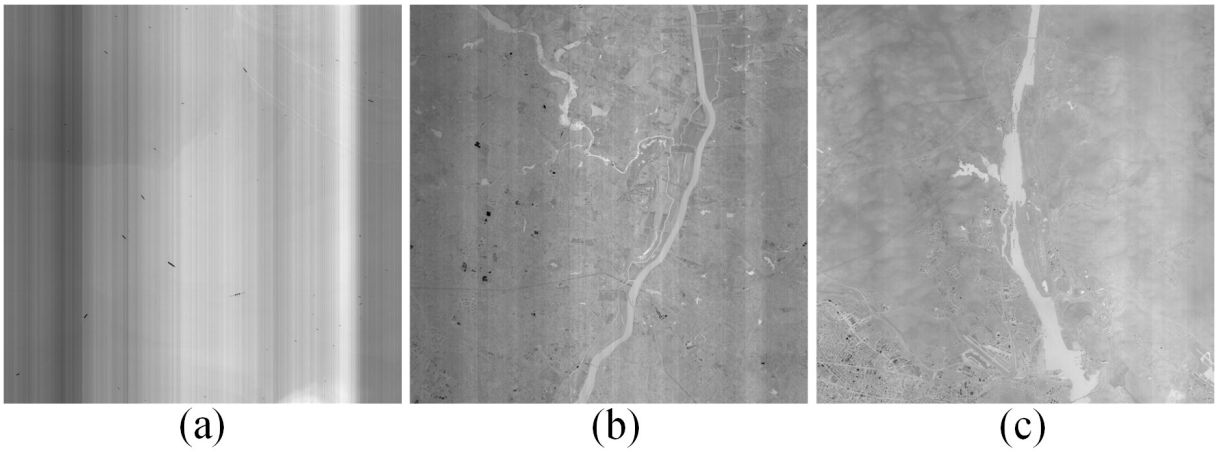


Fig. 11. Original remote sensing images. (a) Harbor. (b) River. (c) Canal.

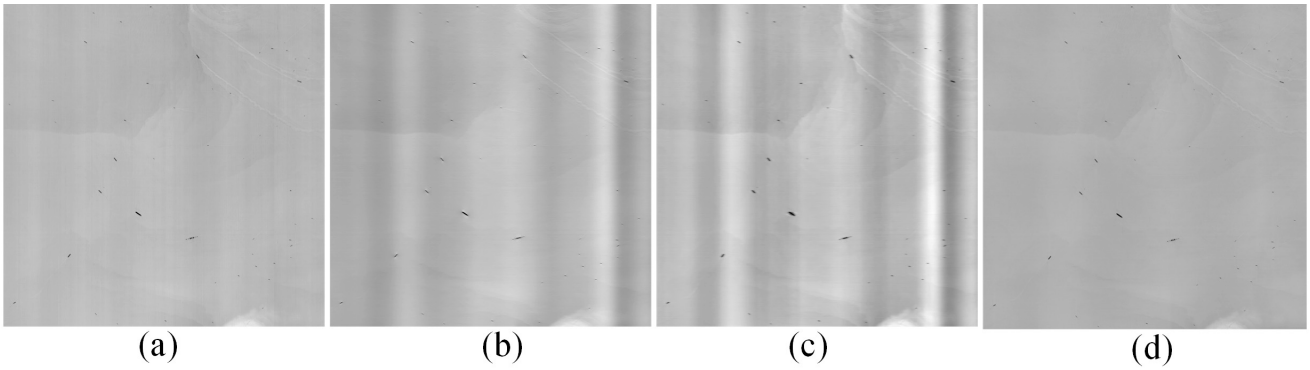


Fig. 12. Efficient and accurate solution in the real-data experiment. (a) UTV+GF. (b) ASSTV+GF. (c) LRID+GF. (d) Proposed.

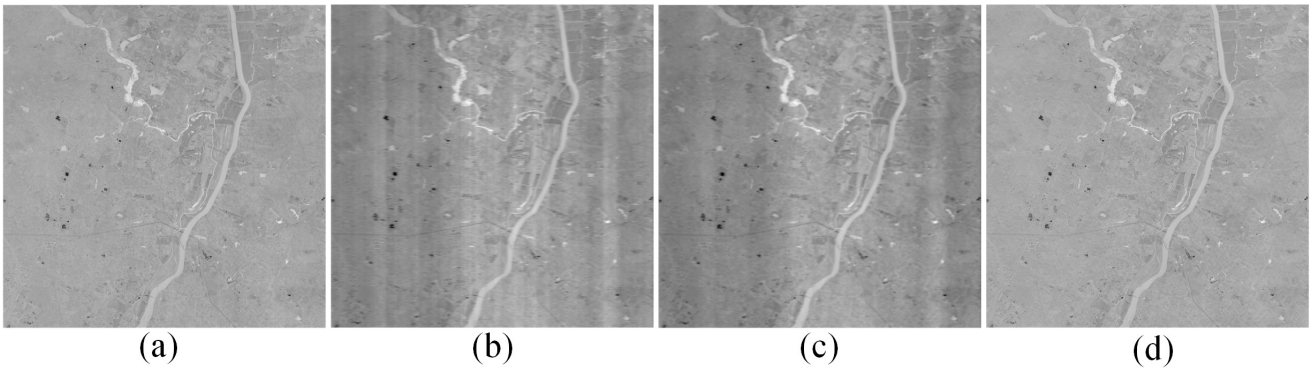


Fig. 13. Efficient and accurate solution in the real-data experiment. (a) UTV+GF. (b) ASSTV+GF. (c) LRID+GF. (d) Proposed.

The ℓ_2 norm for our data fidelity term in (7) implies a Gaussian noise assumption. From this perspective, we see that the scalar weight η_0 should be proportional to the inverse noise variance for each degraded image. To estimate a standard deviation, the median absolute deviation is used in this article. This estimator is useful for sparse signals, such as wavelet-transformed images, because the wavelet coefficients in the finest subbands have only small amounts of signal power. The estimated noise standard deviation σ_n using the robust median estimator is given in [34] as

$$\sigma_n = \frac{\text{Median}(|W_{\text{HH}}|)}{0.6745} \tag{30}$$

where W_{HH} is the set of detail wavelet coefficients of the degraded image in the finest subband with diagonal direction. Therefore, η_0 can be estimated automatically using the above method. In addition, since the noise levels of mixed nonuniformity vary a lot, the functioning degree of the local and global constraints must be adjusted carefully according to the regularization parameters η_1 and η_2. For a more accurate estimation, the regularization parameters were set empirically with the range [50,80] for η_1 and [0.5,1] for η_2. For the penalty parameters, it can be observed in all the experiments that the choice of penalty parameter does not greatly affect the convergence of the SBIA. Thus, α, β, and γ were set empirically until the corrected image obtained the best quality.

Authorized licensed use limited to: XIDIAN UNIVERSITY. Downloaded on February 28,2020 at 03:05:26 UTC from IEEE Xplore. Restrictions apply.

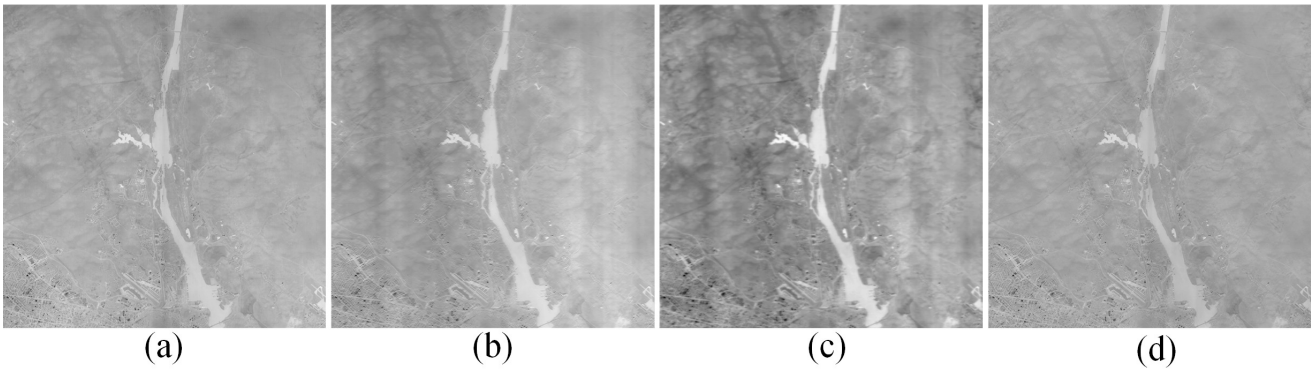


Fig. 14. Efficient and accurate solution in the real-data experiment. (a) UTV+GF. (b) ASSTV+GF. (c) LRID+GF. (d) Proposed.

TABLE III
ICVs OF THE IMAGES CORRECTED BY DIFFERENT NUC ALGORITHMS

Image	Method	Image Patch			
		A	B	C	D
Harbor	Degraded	21.72	20.75	21.29	21.29
	UTV+GF	223.40	207.51	258.74	225.20
	ASSTV+GF	108.64	98.83	104.51	106.02
	LRID+GF	103.81	100.69	99.60	107.09
	Proposed	**314.67**	**313.52**	**312.83**	**295.18**
River	Degraded	7.04	7.64	7.54	8.62
	UTV+GF	14.20	14.54	15.93	17.57
	ASSTV+GF	7.87	8.58	8.42	9.52
	LRID+GF	11.17	12.50	12.03	14.23
	Proposed	**14.46**	**15.34**	**16.29**	**17.84**
Canal	Degraded	10.90	9.89	10.81	9.47
	UTV+GF	20.17	13.62	21.59	14.24
	ASSTV+GF	11.69	10.52	11.53	10.14
	LRID+GF	16.12	13.08	16.24	13.95
	Proposed	**20.88**	**14.97**	**23.62**	**15.56**

More importantly, to estimate the intensity bias of the image background, a significant advantage of our method is to adaptively determine the smoothness degree. The optimal K value has been discussed in [2]. Thus, K is equal to 8 in all the experiments.

2) Running Time: The SBIA is introduced to solve the resulting minimization problem in order to reduce the large computation load. The complex optimization model is decomposed into two independent subproblems that can be calculated or updated in parallel. Moreover, to estimate the latent image, the efficient fast Fourier transform (FFT) is used to solve the corresponding quadratic minimization problem in (22). Consequently, the proposed method is relatively fast. For a 320×256 image, the average running time is about 1.7 s. All the experiments were conducted in MATLAB R2015a on a desktop personal computer with a 3.2-GHz CPU and 16-GB RAM.

V. CONCLUSION

In this article, we have proposed a new NUC model to simultaneously estimate the stripe and intensity bias from low-textured IR noisy images. Different from previous NUC models, the salient characteristics of the stripe component, bias component, and image component have been considered. With the constraints of these properties, the proposed model can precisely separate the mixed noise component and maintain the fine structure of original IR data. In order to solve this nonconvex and nonsmooth optimization model, the SBIA has been applied due to its fast convergence and superior numerical stability. Several simulated and real data sets were tested in our experiments. Both the qualitative and quantitative assessments confirm that the proposed model can output better NUC results than other state-of-the-art techniques of UTV, ASSTV, LRID, and GF.

Although the parametric model works well on various kinds of intensity bias, a great mount of matrix computations are needed in the process of solving the coefficients of parametric bias. To avoid this, a robust nonparametric model may be a better choice, which directs the update of the future work. In addition, horizontal or vertical stripes are removed well by our method, but there are still limitations for oblique stripes in the IR images. Thus, we focus on the higher efficiency and better performance of the optimization model in the future.

REFERENCES

[1] Y. Cao and C.-L. Tisse, "Single-image-based solution for optics temperature-dependent nonuniformity correction in an uncooled long-wave infrared camera," *Opt. Lett.*, vol. 39, no. 3, pp. 646–648, 2014.
[2] L. Liu and T. Zhang, "Optics temperature-dependent nonuniformity correction via ℓ_0-regularized prior for infrared imaging systems," *IEEE Photon. J.*, vol. 8, no. 5, Oct. 2016, Art. no. 3900810.
[3] T. Orżanowski, "Modified two-point calibration algorithm for infrared focal plane arrays," *Proc. SPIE*, vol. 10433, Oct. 2017, Art. no. 104330J.
[4] J.-J. Pan and C.-I. Chang, "Destriping of Landsat MSS images by filtering techniques," *Photogramm. Eng. Remote Sens.*, vol. 58, no. 10, pp. 1417–1423, Oct. 1992.
[5] B. Munch, P. Trtik, F. Marone, and M. Stampanoni, "Stripe and ring artifact removal with combined wavelet—Fourier filtering," *Opt. Express*, vol. 17, no. 10, pp. 8567–8591, May 2009.
[6] Y. Cao, M. Y. Yang, and C.-L. Tisse, "Effective strip noise removal for low-textured infrared images based on 1-D guided filtering," *IEEE Trans. Circuits Syst. Video Technol.*, vol. 26, no. 12, pp. 2176–2188, Dec. 2016.
[7] H. Shen and L. Zhang, "A MAP-based algorithm for destriping and inpainting of remotely sensed images," *IEEE Trans. Geosci. Remote Sens.*, vol. 47, no. 5, pp. 1492–1502, May 2009.
[8] M. Bouali and S. Ladjal, "Toward optimal destriping of MODIS data using a unidirectional variational model," *IEEE Trans. Geosci. Remote Sens.*, vol. 49, no. 8, pp. 2924–2935, Aug. 2011.

Authorized licensed use limited to: XIDIAN UNIVERSITY. Downloaded on February 28,2020 at 03:05:26 UTC from IEEE Xplore. Restrictions apply.

[9] M. Bouali and A. Ignatov, "Estimation of detector biases in MODIS thermal emissive bands," *IEEE Trans. Geosci. Remote Sens.*, vol. 51, no. 7, pp. 4339–4348, Jul. 2013.
[10] Y. Chang, L. Yan, H. Fang, and H. Liu, "Simultaneous destriping and denoising for remote sensing images with unidirectional total variation and sparse representation," *IEEE Geosci. Remote Sens. Lett.*, vol. 11, no. 6, pp. 1051–1055, Jun. 2014.
[11] Y. Chang, L. Yan, T. Wu, and S. Zhong, "Remote sensing image stripe noise removal: From image decomposition perspective," *IEEE Trans. Geosci. Remote Sens.*, vol. 54, no. 12, pp. 7018–7031, Dec. 2016.
[12] F. Pérez, J. E. Pezoa, M. Figueroa, and S. N. Torres, "Empirical frequency domain model for fixed-pattern noise in infrared focal plane arrays," *Infr. Phys. Technol.*, vol. 67, pp. 413–426, Nov. 2014.
[13] A. D. Restrepo-Girón and H. Loaiza-Correa, "Background thermal compensation by filtering for contrast enhancement in active thermography," *J. Nondestruct. Eval.*, vol. 35, no. 1, pp. 1–20, Mar. 2016.
[14] M. M. George, S. Kalaivani, and M. S. Sudhakar, "A non-iterative multi-scale approach for intensity inhomogeneity correction in MRI," *Mag. Reson. Imag.*, vol. 42, pp. 43–59, Oct. 2017.
[15] L. Sripragash and M. Sundaresan, "Non-uniformity correction and sound zone detection in pulse thermographic nondestructive evaluation," *NDT&E Int.*, vol. 87, pp. 60–67, Apr. 2017.
[16] Y. Li, W. Jin, and Z. Liu, "Interior radiation noise reduction method based on multiframe processing in infrared focal plane arrays imaging system," *IEEE Photon. J.*, vol. 10, no. 5, Sep. 2018, Art. no. 6803512.
[17] Y. Chang, L. Yan, L. Liu, H. Fang, and S. Zhong, "Infrared aerothermal nonuniform correction via deep multiscale residual network," *IEEE Geosci. Remote Sens. Lett.*, vol. 16, no. 7, pp. 1120–1124, Jul. 2019, doi: 10.1109/LGRS.2019.2893519.
[18] X. Liu, H. Shen, Q. Yuan, X. Lu, and C. Zhou, "A universal destriping framework combining 1-D and 2-D variational optimization methods," *IEEE Trans. Geosci. Remote Sens.*, vol. 56, no. 2, pp. 808–822, Feb. 2018.
[19] Y. Zheng, S. Lin, S. B. Kang, R. Xiao, J. C. Gee, and C. Kambhamettu, "Single-image vignetting correction from gradient distribution symmetries," in *IEEE Trans. Pattern Anal. Mach. Intell.*, vol. 35, no. 6, pp. 1480–1494, Jun. 2013.
[20] X. Lan, H. Shen, L. Zhang, and Q. Yuan, "A spatially adaptive Retinex variational model for the uneven intensity correction of remote sensing images," *Signal Process.*, vol. 101, pp. 19–34, Aug. 2014.
[21] N. J. W. Morris, S. Avidan, W. Matusik, and H. Pfister, "Statistics of infrared images," in *Proc. IEEE Conf. Comput. Vis. Pattern Recognit.*, Minneapolis, MN, USA, Jun. 2007, pp. 1–7.
[22] T. R. Goodall, A. C. Bovik, and N. G. Paulter, "Tasking on natural statistics of infrared images," *IEEE Trans. Image Process.*, vol. 25, no. 1, pp. 65–79, Jan. 2016.
[23] R. M. H. Nguyen and M. S. Brown, "Fast and effective L_0 gradient minimization by region fusion," in *Proc. IEEE Conf. Comput. Vis. Pattern Recognit.*, Boston, MA, USA, Dec. 2015, pp. 208–216.
[24] J. Pan, Z. Hu, Z. Su, and M.-H. Yang, "L_0-regularized intensity and gradient prior for deblurring text images and beyond," *IEEE Trans. Pattern Anal. Mach. Intell.*, vol. 39, no. 2, pp. 342–355, Feb. 2017.
[25] H. Shen *et al.*, "Missing information reconstruction of remote sensing data: A technical review," *IEEE Geosci. Remote Sens. Mag.*, vol. 3, no. 3, pp. 61–85, Sep. 2015.
[26] M. V. Afonso, J.-M. Bioucas-Dias, and M. A. T. Figueiredo, "Fast image recovery using variable splitting and constrained optimization," *IEEE Trans. Image Process.*, vol. 19, no. 9, pp. 2345–2356, Sep. 2010.
[27] T. Goldstein, X. Bresson, and S. Osher, "Geometric applications of the split Bregman method: Segmentation and surface reconstruction," *J. Sci. Comput.*, vol. 45, no. 1, pp. 272–293, Oct. 2010.
[28] T. Qiao, W. Li, B. Wu, and J. Wang, "A chaotic iterative algorithm based on linearized Bregman iteration for image deblurring," *Inf. Sci.*, vol. 272, pp. 198–208, Jul. 2014.
[29] R. Campagna, S. Crisci, S. Cuomo, L. Marcellino, and G. Toraldo, "Modification of TV-ROF denoising model based on split Bregman iterations," *App. Math. Comput.*, vol. 315, pp. 453–467, Aug. 2017.
[30] L. Xu, C. Lu, Y. Xu, and J. Jia, "Image smoothing via L_0 gradient minimization," *ACM Trans. Graph.*, vol. 30, no. 6, pp. 174:1-174:11, 2011.
[31] Y. Chang, L. Yan, H. Fang, and C. Luo, "Anisotropic spectral-spatial total variation model for multispectral remote sensing image destriping," *IEEE Trans. Image Process.*, vol. 24, no. 6, pp. 1852–1866, Jun. 2015.
[32] Z. Wang and A. C. Bovik, "Mean squared error: Love it or leave it? A new look at signal fidelity measures," *IEEE Signal Process. Mag.*, vol. 26, no. 1, pp. 98–117, Jan. 2009.
[33] G. Smith and P. Curran, "Methods for estimating image signal-to-noise ratio (SNR)," in *Advances in Remote Sensing and GIS Analysis*, P. Atkinson and N. Tate, Eds. Hoboken, NJ, USA: Wiley, 2000, pp. 61–74.
[34] B. G. Jeong, B. C. Kim, Y. H. Moon, and I. K. Eom, "Simplified noise model parameter estimation for signal-dependent noise," *Signal Process.*, vol. 96, pp. 266–273, Mar. 2014.



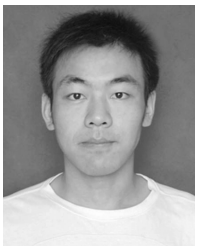
Li Liu received the Ph.D. degree in control science and technology from the Huazhong University of Science and Technology, Wuhan, China, in 2016.

He has been an Assistant Professor with Xidian University, Xi'an, China, since 2016. His main research interests include infrared image correction, image deblurring, image enhancement, and object detection and recognition.



Luping Xu received the Ph.D. degree in signal and information processing from Xidian University, Xi'an, China, in 1996.

Since 2000, he has been a Professor with Xidian University. His main research interests are target detection, spread spectrum, satellite and mobile communications, and SAR image processing.



Houzhang Fang received the M.S. and Ph.D. degrees in applied mathematics and control science from the Huazhong University of Science and Technology, Wuhan, China, in 2010 and 2014, respectively.

He is currently a Lecturer with Xidian University, Xi'an, China. His research interests include image restoration, blind image deconvolution, and object detection and recognition.

Authorized licensed use limited to: XIDIAN UNIVERSITY. Downloaded on February 28,2020 at 03:05:26 UTC from IEEE Xplore. Restrictions apply.